Fluidics Thrust Vectoring Using Co-Flow Method

Ali Abdul Almuhsen Al-Asady
Department of Mechanical Engineering
College of Engineering
Baghdad University

Ahmed Mujahid Abdullah
Department of Mechanical Engineering
College of Engineering
Baghdad University

Abstract

Computational and experimental investigations of thrust vectoring using co flow method had been carried in the present work. The experimental investigation included design and construction of rig with rectangular duct with aspect ratio (4.4) in order to investigate the effect of various geometric variables on thrust vectoring angle. Set of experiments tests carried out over the mass flow ratio ($\dot{m}s/\dot{m}p$) range $0 \leq \dot{m}s/\dot{m}p \leq 0.23$, gap height h/H= (0.0294, 0.0588, 0.088 and 0.1176) and coanda surface diameter Φ/H= (1.176, 2.353 and 3.529).

Load measurements were obtained using four load cells. The computational investigation involved a 3D numerical solution by FLUENT 6.3.26 Software for some of experimental cases. The results show that the increase in secondary jet blowing rate lead to increase the jet vectoring angle, there are three zone can be observed, dead zone appears at low mass flow ratios, then followed by control region in which continuous thrust vector control can be achieved followed by a saturation region. The coanda surface diameter determines the length of the dead zone, which a small coanda surface used for coanda effect resulted in a prolonged dead zone range and the secondary gap height to the primary gap height had inverse relation with jet vectoring angle. The investigation shows that both the experimental and computational results obtained follow a similar trend line.

Keywords: Thrust vectoring, Jet vectoring, Coanda Effect, Co-Flow, Fluid injection

Nomenclature:

Symbol	Definition	Units
H	Height of Primary Jet	mm
g	Gap height of Secondary Jet	mm
k	the turbulent kinetic energy	
L	length of Primary Jet	mm
$\dot{M}$p	Primary Mass Flow Rate	Kg/s
$\dot{M}$s	Secondary Mass Flow Rate	Kg/s
P_b	The generation of turbulence kinetic energy due tobuoyancy.	
P_k	The generation of turbulence kinetic energy due to the mean velocity gradients	
S	the modulus of the mean rate-of-strain tensor	
Φ	Coanda Surface Diameter	mm
Fx	Horizontal Force	kg
Fy	Vertical Force	kg
Vp	velocity of primary flow	m/s
Vs	velocity of secondary flow	m/s
$\bar{u}$	Average Velocity in x Axes	m/s
$\grave{u}$	Fluctuations Velocity in x Axes	
$\bar{v}$	Average Velocity in y Axes	m/s
$\grave{v}$	Fluctuations Velocity in y Axes	
W	Width of Primary Jet	mm
$\bar{w}$	Average Velocity in z Axes	m/s
$\grave{w}$	Fluctuations Velocity in z Axes	
δ	Thrust Vectoring Angle	degree
ρ	Density	kg/m^3
μ_t	the turbulent viscosity	
3-D	Three Dimension	
CFD	Computational Fluid Dynamics	
CFTV	Counter flow thrust vectoring	
FTV	Fluidic thrust vectoring	
MTV	Mechanical thrust vectoring	
$C_{1\varepsilon}$	Model constant = 1.44	
$C_{2\varepsilon}$	Model constant = 1.92	
$C_{3\varepsilon}$	Model constant = -0.33	
Cμ	Model constant = 0.09	
σ_ε	Model constant = 1.3	
σ_k	Model constant = 1.0	

1. Introduction

The ability to redirect the thrust of an aircraft engine or rocket exhaust offers several advantages to the aerospace industry. It provides the potential for a vertical component of thrust which may be used, especially at low speeds, to augment the lift force generated by the wings. This allows the aircraft to take off in a shorter distance, and ascend at a higher

rate. During landing, vectored thrust can be used to supplement the lift force generated by the wings, and approach speeds may be reduced without changing the rate of descent. The benefits of short takeoff and landing aircraft are especially attractive for landing on aircraft-carriers or on damaged airfields.

Traditionally the wings are the sole mechanism for generating lift. However they have aerodynamic limitations, namely airfoil stall, which causes a dramatic decrease in airfoil performance and must be avoided to maintain adequate control of the aircraft. Thrust vectoring can be used to maintain or re-establish control under stalled conditions, thus enhancing the overall maneuverability of the plane. In missile applications, multiaxis thrust vector control could be employed for steering control at potentially considerably lower expense in terms of vehicle weight and cost, **[6]**.

When a jet of fluid emerges from a nozzle, it continues to move downstream and is not deflected in one direction or other. It is found that the motion of the jet entrains particles from the surroundings fluid causing it to spread out as it moves downstream. If the entrainment flow on one side of the jet is reduced due to the existence of an adjacent wall, the pressure on that side of the jet is reduced due to differential entrainment, causing the jet to be drawn toward the low pressure region, **[3]**, **Fig. 1**.

In free surroundings, a jet of fluid entrains and mixes with its surroundings as it flows away from a nozzle. When a surface is brought close to the jet, this restricts the entrainment in that region. As flow accelerates to try balance the momentum transfer, a pressure difference across the jet results and the jet is deflected closer to the surface - eventually attaching to it. Even if the surface is curved away from the initial direction, the jet tends to remain attached. This effect can be used to change the jet direction. In doing so, the rate at which the jet mixes is often significantly increased compared with that of an equivalent free jet, (www.thermofluids.co.uk/effect.php).

Fluidic thrust vectoring system relies on a phenomenon known as Coanda effect. It states that fluid and gases jets have a natural tendency to attach to the wall, which is projected close to them and follow the convex curvature of the solid boundary. The principle was named after Romanian aerodynamicist inventor Henri-Marie Coanda, 1930, who was the first to understand the practical importance of the phenomenon for aircraft development. In order to describe this phenomenon, the tangential jet sheet which exits over the curved surface is supposed. This curvature can turn through a full 180° or more. The jet remains attached to that curved surface because of a balance between the sub ambient pressure in the jet sheet and the centrifugal force in the jet going around the curvature. Initially, at very low blowing values, the jet entrains the boundary layer to prevent aft flow separation and is thus a very effective boundary layer control is achieved. Eventually, as the jet continues to turn, a rise in the static pressure plus viscous shear stress and centrifugal force combine to separate the jet sheet and a new stagnation point and stagnation streamline are formed on the trailing edge of the Coanda surface.

1.1 Types of Thrust Vectoring:

Fluidic control techniques can be categorized into five basic types, namely; counter-flow, co-flow, shock vector control, synthetic jet actuator and throat shifting.

- Both the counter flow and co-flow concepts involve the use of a secondary jet in addition to the Coanda effect to facilitate thrust vectoring. The former technique uses momentum removal whereas the latter uses momentum injection to control the primary jet, **[2]**, **Fig. 2**.
- Shock thrust vector control involves injecting a secondary jet into the primary jet from one of the divergent flaps. An oblique shock wave is formed which deflects the primary jet in the pitch plane, **[2]**. Fluidic thrust vectoring with the shock vector control method requires forced, asymmetric fluidic injection of a secondary air stream into the supersonic, primary flow that develops in the divergent section of the nozzle at certain conditions, **[8]**, **Fig. 3**.
- Throat shifting methods utilizes fluidic injection at the nozzle throat to turn the subsonic flow ahead of the nozzle throat, subsonic flow turning incurs lower losses than supersonic flow turning. Therefore, throat shifting methods typically achieve higher system thrust ratios than shock-vector control methods, **[1]**, **Fig. 4**.
- Miniature fluidic actuator that provided spatially distributed mass addition with advances in miniaturization and micro fabrication techniques. There is now the ability to integrate these microfluidic devices into the body of nozzles or aerodynamic surfaces with minimal obtrusiveness. The fluidic actuator had all feedback passages built into the nozzle body.

  Fluidic excitation devices are potentially useful for shear flow control for several reasons: they have no moving parts; they can produce excitation that is controllable in frequency, amplitude and phase. They can operate in harsh thermal environments, which are not susceptible to electromagnetic interference, and are easy to integrate into a functioning device, **[5]**, **Fig. 5**.

2. Objective of Present Work

Experimental and numerical study for thrust vectoring using secondary jet in parallel with primary jet applying co flow method is carried out in the present work. The following points are to be investigated**:**

- Numerical solution of some experimental cases is achieved by using FLUNET program to investigate the effect of various parameters, secondary gap height (h) and coanda surface diameter (Φ).
- Experimental work is made to investigate the problem and explore the effect of various parameters, secondary gap height (h) and coanda surface diameter (Φ).
- Parametric investigation for a number of affecting parameters, such as coanda surface diameter, secondary gap slot height and secondary flow rate.

3. Experimental Work:

An experimental rig was designed and constructed in the Heat Transfer Lab, at the Mechanical Engineering Department, University of Baghdad. The rig was designed and built in order to investigate the effect of various geometric variables on thrust vectoring effectiveness. These included secondary gap height (h) and Coanda surface diameter, Φ.The experimental rig is shown in **Fig. 6**.

3.1 Test Section:

The test section Consists of rectangular duct, this duct was made of aluminum with width of W=75 mm, height of H=17 mm and length of L= 750 mm, utilizing different compatible secondary Coanda surfaces. A total of three flaps with different configurations were examined in order to investigate the effects of varying collar diameter Φ=20 mm, 40 mm, and 60 mm (Φ/H= 1.176, 2.353, and 3.529) into the thrust-vectoring performance shown in **Fig. 7**, these flaps were made of aluminum with length of 15mm and box with four air intake openings to deliver a uniform flow to the secondary slot. Furthermore, four different secondary slot heights h= 0.5 mm, 1 mm, 1.5 mm and 2 mm (h/H= 0.0294, 0.0588. 0.088, 0.1176), and six different secondary air mass flows were tested for each flap in a specific main jet speed. By positioning the Coanda surface at the exit of the primary nozzle and introducing the secondary stream of co-flowing air, parallel to the Coanda surface, co-flow fluidic thrust vectoring can be obtained. The test section was attached to a centrifugal blower with constant volume rate equal to 11 $m^3/\min$ and pressure equal to 1.1 bars to provide the primary jet flow. The secondary jet flow was provided by reciprocating compressor which connected to cylindrical container with capacity of 500 litters and provide volume flow rate equal to 0.4 $m^3/\min$.

The secondary mass flow rates were controlled using a pressure regulator with flow rates measured using a flow meter calibrate in the lab see **Fig. 8**. The thrust vectoring angle obtained by **eq. (1)**

$$\delta = \tan^{-1}(Fy/Fx) \quad (1)$$

Vertical and horizontal forces were measured by using two sets of balanced load cells, one for horizontal force along the duct axis and the other for vertical force perpendicular to the duct. **Fig. 6**.

3.2 The Experimental Procedure:

1. Assign the coanda surface on the rectangular duct.
2. Specify the slot high which be used for the run by using block gauge.
3. Make sure there is no leak or obstacle in the air stream.
4. Attached the center line of the duct with two load cells vertically by two link and the sides of the duct with two load cells horizontally, so the duct is balanced and free to move.
5. Turn on the power supply then the weight indicator.
6. Make sure that the test section is in equilibrium and the indicator value at zero.
7. Turn on the blower and adjust the valve to get a specify primary air flow which is measured by vane type anemometer.
8. Turn on the compressor and adjust the regulator valve to a specific pressure.
9. Control the secondary air flow by adjusting a ball valve and record the volume rate which is measured by the flow meter.
10. Repeat the steps from 2 to 9 for other secondary slot high.
11. Repeat the steps from 1 to 10 for other coanda surfaces diameter.

4. CFD Simulation:

A computational investigation for 3D flow was undertaken primarily to aid in the design of the experimental rigs. A solution of **Navier-stokes** equations and the standard k-ε turbulence model was used to simulate the jet flows in this study. Using a **CFD Code FLUENT 6.3.26** after describing the model using **GAMBIT 2.2.30**, the computational domain was created using an unstructured meshing scheme consisting of tetrahedral elements. The effects of Coanda surface geometry and secondary gap height on vectoring angle for increasing secondary jet blowing rates were investigated. The CFD simulations provided force data which were then compared to the experimental data obtained.

4.1 System and Model Geometry

The system geometry in the present work basically consists of multi boxes, which represents the room and the model. The room was presented by a box with dimension of X=800mm * Y=600mm * Z=400mm.

The original design geometry consists of primary duct, secondary duct and coanda surface. It is identical to the passage generated in the experimental test rig which will be introduced in chapter four. The geometry is generated by using **GAMBIT** as three geometries with specific locations, interconnecting them by some interrelationships prepared for meshing and boundary conditions specifications.

The geometry of the present model is show in plate (1) It consists of:

- The primary duct with dimensions of L=750 mm * W=75mm * H=17mm.
- The secondary with dimensions of L=200mm* W=75mm *h=0.5mm, 1mm, 1.5mm and 2mm respectively.
- The coanda surface with dimensions of W=75mm *R=2cm, 4cm and 6cm.

  Also, the two regions are interconnected with split function so the analysis of the results are continuum and interchangeable in between of them.

4.2 Assumptions

The working fluid is Air and the flow characteristics are assumed to have the following assumptions:

- Three dimensional
- Steady flow
- No heat source
- Incompressible fluid (due to low flow velocity ; Mach number is less than 0.3)
- Turbulent flow

4.3 Governing Equations

Conservation equations are continuity and momentum for turbulent model of the flow is presented in FLUENT built – in solver. It is important here to refer back and discuss the general conservations equations as follows:

Continuity equation:

$$\frac{\partial \rho}{\partial t} + \nabla.(\rho\, \vec{v}) = 0 \qquad \dots \quad (2)$$

Where:

$\vec{v}$: is the velocity vector.

For incompressible flow (ρ=constant) and the equation above is simplified to be:

$$\nabla.\vec{v} = 0 \qquad \dots \quad (3)$$

Momentum equation:

$$\frac{\bar{u}\partial\bar{u}}{\partial x} + \frac{\bar{v}\partial\bar{u}}{\partial y} + \frac{\bar{w}\partial\bar{u}}{\partial z} = -\frac{1}{\rho}\frac{\partial\bar{p}}{\partial x} + \nu(\nabla^2\bar{u}) - \frac{\partial\overline{(\dot{u})^2}}{\partial x} - \frac{\partial\overline{(\dot{u}\dot{v})}}{\partial y} - \frac{\partial\overline{(\dot{u}\dot{w})}}{\partial z} \qquad \dots \quad (4)$$

$$\frac{\bar{u}\partial\bar{v}}{\partial x} + \frac{\bar{v}\partial\bar{v}}{\partial y} + \frac{\bar{w}\partial\bar{v}}{\partial z} = -\frac{1}{\rho}\frac{\partial\bar{p}}{\partial y} + \nu(\nabla^2\bar{v}) - \frac{\partial\overline{(\dot{u}\dot{v})}}{\partial x} - \frac{\partial\overline{(\dot{v})^2}}{\partial y} - \frac{\partial\overline{(\dot{v}\dot{w})}}{\partial z} \qquad \dots \quad (5)$$

$$\frac{\bar{u}\partial\bar{w}}{\partial x} + \frac{\bar{v}\partial\bar{w}}{\partial y} + \frac{\bar{w}\partial\bar{w}}{\partial z} = -\frac{1}{\rho}\frac{\partial\bar{p}}{\partial z} + \nu(\nabla^2\bar{w}) - \frac{\partial\overline{(\dot{u}\dot{w})}}{\partial x} - \frac{\partial\overline{(\dot{w}\dot{v})}}{\partial y} - \frac{\partial\overline{(\dot{w})^2}}{\partial z} \qquad \dots \quad (6)$$

Where:

$$\nabla^2 = \frac{\partial^2}{\partial x^2} + \frac{\partial^2}{\partial y^2} + \frac{\partial^2}{\partial z^2} \qquad \dots \quad (7)$$

The $\mathbf{k-\epsilon}$ turbulence model equation:

The turbulent kinetic energy **k** equation is written as:

$$\frac{\partial}{\partial t}(\rho k) + \frac{\partial}{\partial x_i}(\rho k u_i) = \frac{\partial}{\partial x_j}\left[\left(\mu + \frac{\mu_t}{\sigma_k}\right)\frac{\partial k}{\partial x_j}\right] + P_k + P_b - \rho\epsilon - Y_M + S_k \qquad \dots \quad (8)$$

For dissipation **ϵ** equation is written as:

$$\frac{\partial}{\partial t}(\rho\epsilon) + \frac{\partial}{\partial x_i}(\rho\epsilon u_i) = \frac{\partial}{\partial x_j}\left[\left(\mu + \frac{\mu_t}{\sigma_\epsilon}\right)\frac{\partial\epsilon}{\partial x_j}\right] + C_{1\epsilon}\frac{\epsilon}{k}(P_k + C_{3\epsilon}P_b) - C_{2\epsilon}\rho\frac{\epsilon^2}{k} + S_\epsilon \qquad \dots \quad (9)$$

5. Experamental Results and Disscution:

A systematic series of tests were carried out in order to investigate the effect of various geometry variables and flow condition on thrust vectoring angle. These included secondary gap height (*h*), Coanda surface diameter (Φ) and secondary flow rate ($\dot{m}_s$).

5.1 Varying Secondary Gap Height (h/H):

Fig. 9 shows the relationship between the mass flow ratio $\dot{m}s/\dot{m}p$ (secondary flow rate/ primary flow rate) and the resulting thrust vector angle for various secondary gap heights at a constant Coanda surface diameter of Φ/*h* = 1.176. Four secondary gap heights were tested h/H= (0.0294, 0.0588. 0.088, 0.1176). The results show that as the secondary jet blowing rate is increased, the thrust vector angle value increased to maximum value equal to (28.37) degree. It can be seen that as the secondary gap height value increased, the values obtained for vectoring angle decrease from maximum value (28.37) degree for h/H = 0.0294 to maximum value (24) degree for h/H = 0.1176.

Fig. 10 & 11 show the relation between

($\dot{m}s/\dot{m}p$) and vectoring angle of the tests at constant coanda surface diameter of Φ/*h* = 2.35 and Φ/*h* = 3.53 respectively. The results show that as the secondary jet blowing rate is increased, as the thrust vector angle value increased. It can be seen that as the secondary gap height increases, the values obtained for vectoring angle decrease accordingly at each mass flow ratio tested.

The small gap height leads to smaller cross section area for secondary duct which affect the velocity value at the coanda surface for the same amount of secondary flow rate. High velocity values produce a low pressure region which is responsible for the primary jet vectoring.

The results show that at very low secondary jet blowing rates i.e. $\dot{m}_s \ll \dot{m}_p$ the thrust vector angle is very small and there appears to be a 'dead zone' in which no flow control can be achieved.

At low secondary jet blowing rates, the secondary jet separates early from the Coanda surface. In extreme cases, control reversal can occur (negative vectoring angle) whereby the primary jet vectors in the opposite direction before vectoring in the direction expected. In this instance, the faster moving primary jet entrains the slower moving air of the secondary jet and instead of adhering to the Coanda surface and remaining attached far downstream, the secondary jet separates and a high pressure region forms. The entrainment air has the effect of skewing the primary jet velocity distribution towards the opposite Coanda surface and the differential pressure gradient created vectors the primary jet in that direction due to the high pressure region. After the 'dead zone', the Coanda effect dominates and the curve enters a region in which a large increase in thrust vector angle can be achieved for relatively small increase in the secondary jet blowing rate. In this region, continuous control of the primary jet can be achieved. From now on the thrust vector angle, and hence the thrust vector force generated, will enter a hypothetical region of saturation i.e. the thrust vector angle reaches an almost constant value, for any increase in secondary jet blowing rate.

5.2 Varying Coanda Surface Diameter (Φ/H):

Fig. 12 shows the relationship between the mass flow ratio ($\dot{m}s/\dot{m}p$) and the resulting thrust vectoring angle for various Coanda surface diameters at a constant secondary gap height ratio of h/H= 0.0294. Four cases has been studied, one without Coanda surface and three with coanda surface diameters Φ/H= (1.176, 2.353, and 3.529). As shown in **Fig. 12**, an increase in secondary jet blowing rate results in an increase in the value of vectoring angle, and as the Coanda surface diameter is increased the gradient of the curve becomes steeper once the 'dead zone' has been overcome. The diameter of the Coanda surface also determines the size of the 'dead zone' and hence where the onset of the control region begins.

The results show that the secondary jet is more likely to separate at the center of Coanda surface with a small diameter and as a consequence the 'dead zone' will be prolonged over a wider range of secondary jet blowing rate values, because the large diameters provide a larger surface that fluid will attach to it.

Fig. 13, 14 & **15** show the relation between $\dot{m}s/\dot{m}p$ and vectoring angle of the tests at constant gap height of h/H = 0.0588, 0.088 and 0.1176 respectively. Four Coanda surface diameters were tested Φ/H= (0, 1.176, 2.353, and 3.529) and the result follow the same behavior as Shown in **Fig. 12**

6. Cfd Results:

Six cases have been studied, four varying secondary gap height at constant coanda surface diameter Φ/H= 1.176 and two cases for varying coanda surface diameter at constant secondary gap height h/H = 0.0588, shown in **table 1**. The results directly reported from FLUENT for the resolved F_X and F_Y on the coanda and ducts walls to obtain the jet vectoring.

Fig. 16 shows a CFD simulation for the velocity vectors at Φ /H=1.176, h/H= 0.088 and = 0.098.

7.Comarisons Between Cfd and Experimental Work:

Fig. 19 & **20**, show comparisons between CFD and Experimental results for varying secondary gap height at constant Coanda surface diameter Φ/H= 1.176. It can be seen that both curves for CFD and experimental results follow a similar trend. However, the extent of the 'dead zone' for the experimental work is more prolonged than that obtained in the CFD work. The computational work has also highlighted both the control and saturation regions as seen previously in the experimental results. At low secondary jet blowing rates, the CFD investigation predicted greater thrust vectoring angle than those obtained during the experimental tests for approximately the same mass flow ratio.

8. Conclusions:

The present CFD and experimental investigation of fluidic jet vectoring using co-flow method show several conclusions. These conclusions can be summarized as below:-

1. Both the theoretical and experimental results followed a similar trend. A dead zone appears at

low flow ratio ($\dot{m}s/\dot{m}p$) followed by an active zone when the thrust vectoring can be achieved, then a saturation region appeared in which the thrust vectoring angle reach a constant value for any increase in flow ratio ($\dot{m}s/\dot{m}p$) due to physical limitation.

2. Thrust vectoring angle increased by increasing mass flow ratio ($\dot{m}s/\dot{m}p$), once the dead zone has been overcome.
3. The coanda surface diameter determine the length of the dead zone, the small diameter resulted in prolonged dead zone range and vice versa.
4. Thrust vectoring angle increased, as the secondary gap height decrease for each flow ratio tested.
5. The deference between theoretical an experimental results was due to experimental errors because the generated forces were small and required a very sensitive load cells which is not available.

9. References:

[1] Deere, K.A., Berrier, B.L., Flamme, J.D. and Johnson, S.K., 2005, *Computational Study of Fluidic Thrust Vectoring Using Separation Control in a Nozzle*, American Institute of Aeronautics and Astronautics, vol.2003, issue 3803.

[2] Mason, M.S. and Crowther, W.J., 2002, *Fluidic Thrust Vectoring of Low Observable Aircraft*, CEAS Aerospace Aerodynamic Research Conference.

[3] Morris, N.M., 1973, *An Introduction to Fluid Logic*, McGraw-Hill, Maidenltead, Berkshire. England.

[4] Raman, G., Packiarajan, S., Papadopoulos, G., Weissman, C. and Raghu, S., 2005, *Jet Thrust Vectoring Using a Miniature Fluidic Oscillator*, The Aeronautical Journal, Paper No. 2835, pp.129-138.

[5] Smith, B.L. and Glezer, A., 2001, *Jet Vectoring Using Synthetic Jets*, Journal of Fluid Mechanics, Vol.458, p.p. 1-34.

[6] Strykowski, P.J., 1999, *Vectoring Thrust Using Confined Shear Layers*, Naval Research Reviews, Vol.51 (3, 4).

[7] Web site 1: www.thermofluids.co.uk/effect.php

[8] Zou, H.X. and Wang, Q., 2011, *The Comparative Analysis of Two Typical Fluidic Thrust Vectoring Exhaust Nozzles on Aerodynamic Characteristics*, World Academy of Science, Engineering and Technology, Vol. 76, p.p. 610-616.

[9]Blake B.A., 2009, Numerical investigation of Fluidic Injection as a means of thrust vectoring, M.Sc. Thesis, the University of New South Wales

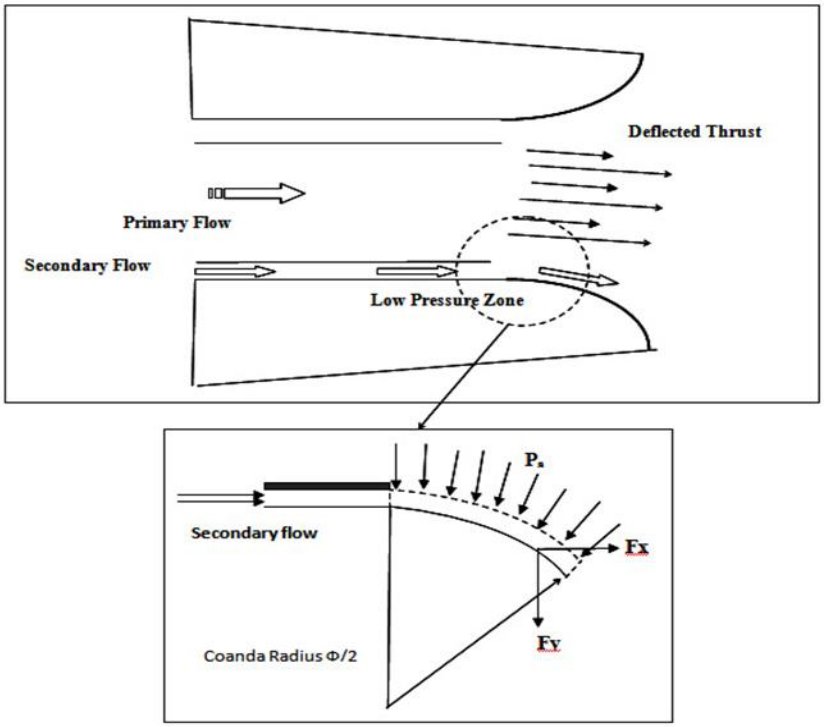

Figure 1 : Schematic diagram of Co-Flow Fluidic Thrust Vectoring [2]

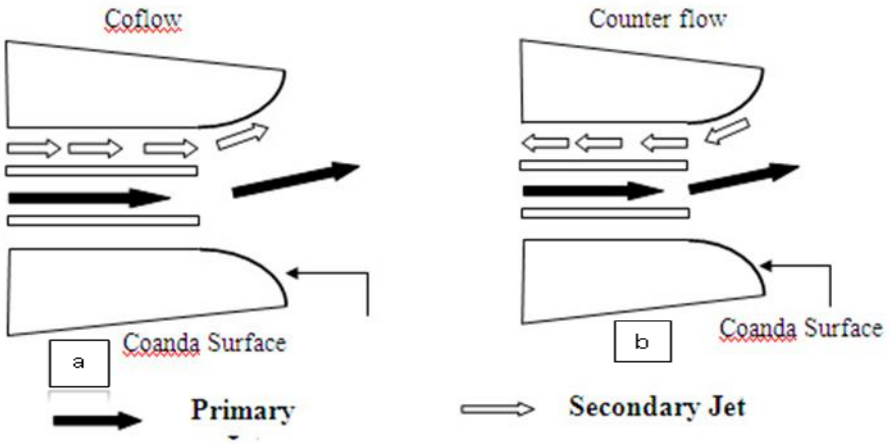

(a) Co- flow (b) Counter flow

Figure 2 : Schematic shows the co-flow and counter flow technique [2]

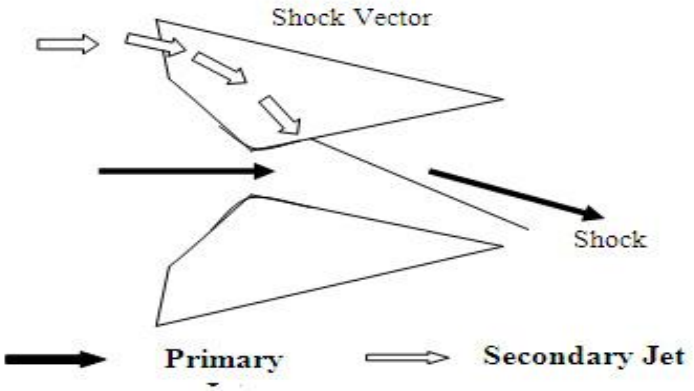

Figure 3 : The shock thrust vector technique [8]

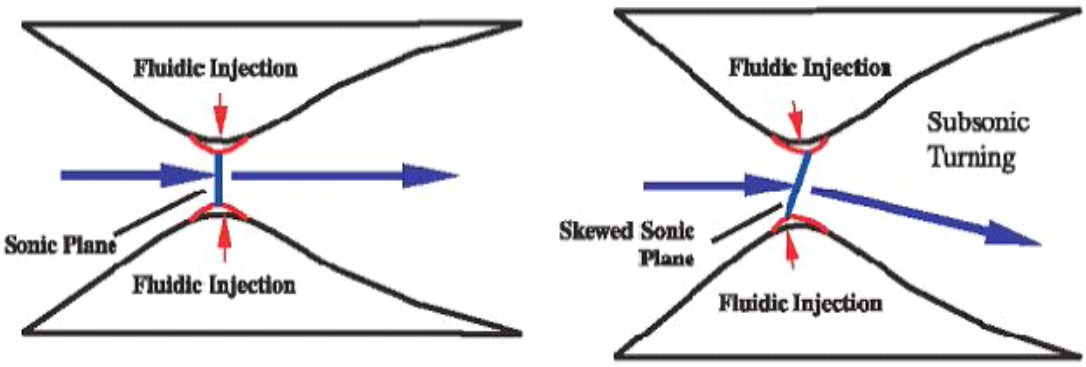

Figure 4 : Schematic diagram show the throat shifting fluidic thrust vectoring technique **[9]**

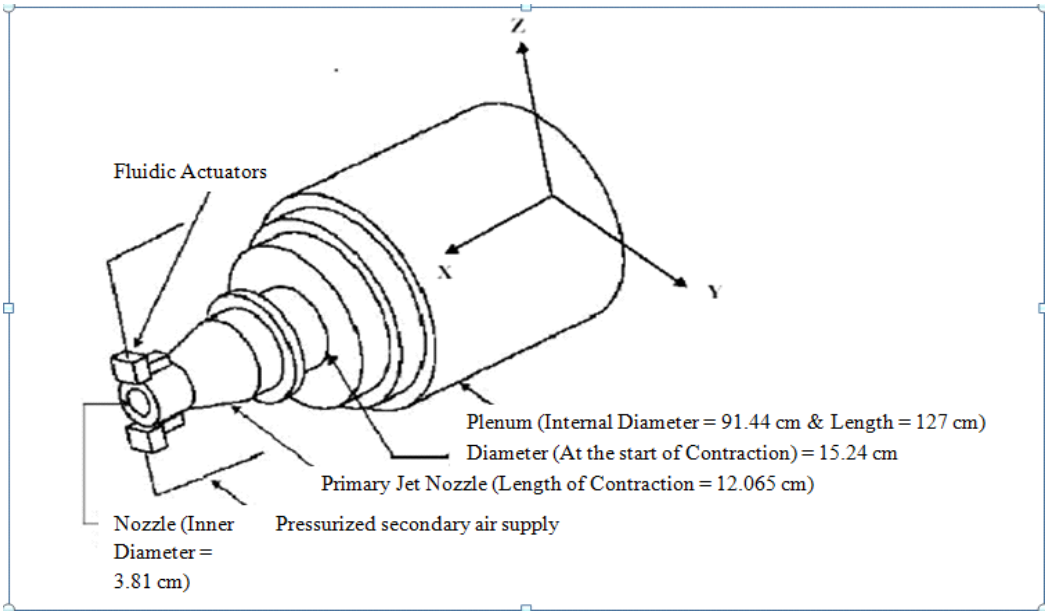

Figure 5 : Schematic diagram shows thrust vectoring using a miniature fluidic actuator [5]

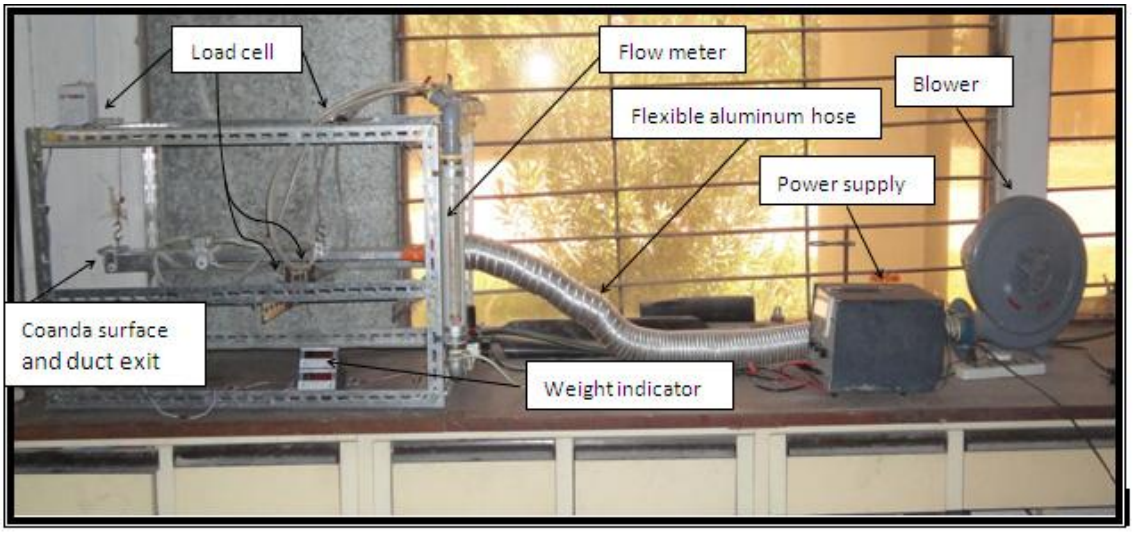

Plate 1: Photograph of the experimental rig

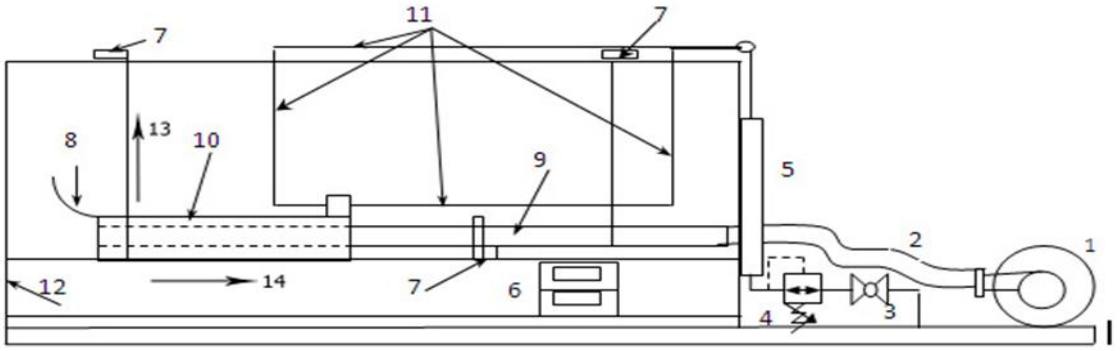

1	Centrifugal Blower	8	Coanda Surface
2	Flexible Hose	9	Main Jet
3	Ball Valve	10	Secondary Jet
4	Regulator Valve	11	Pipes
5	Flow Meter	12	Frame
6	Weight Indicator	13	Fy
7	4 Load Cells	14	Fx

Figure 6: Schematic diagram of the experimental rig

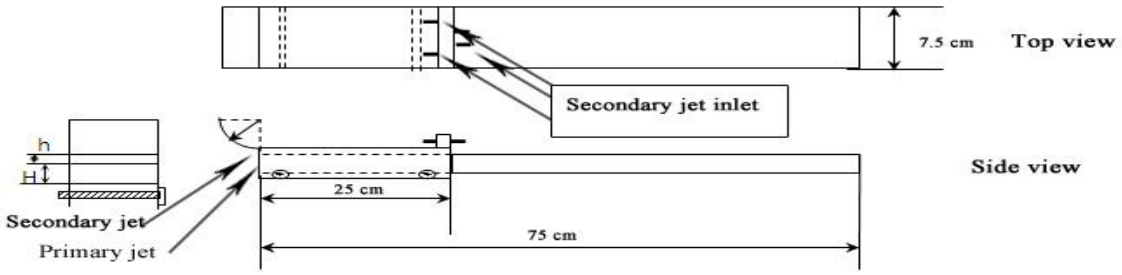

Figure 7: Schematic of the test section

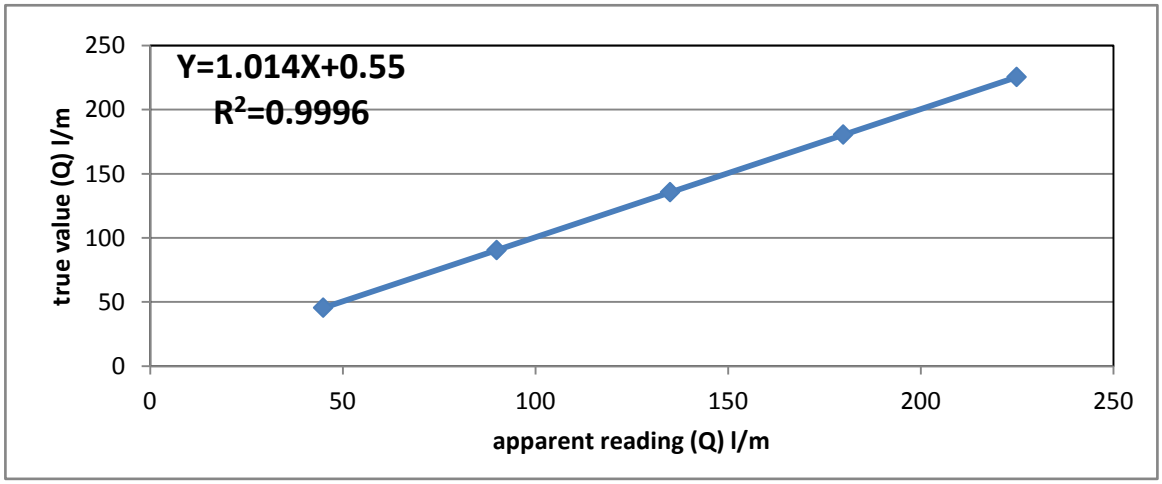

Figure 8: Calibration curve for the flow meter used in the experimental work.

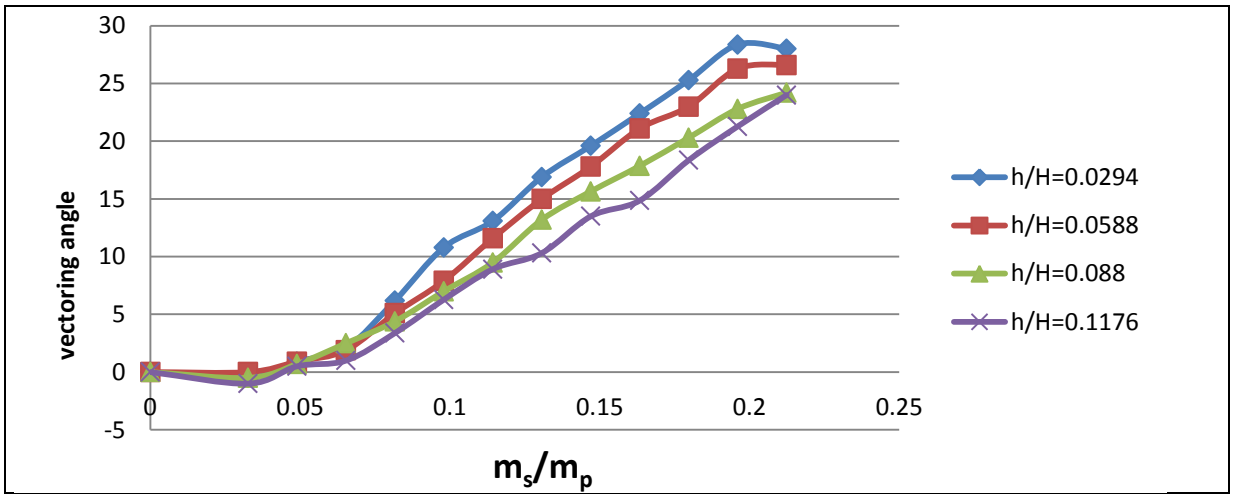

Figure 9 : Experimental results of Thrust vectoring angle for varying secondary gap height at constant Coanda surface diameter Φ/H =1.176

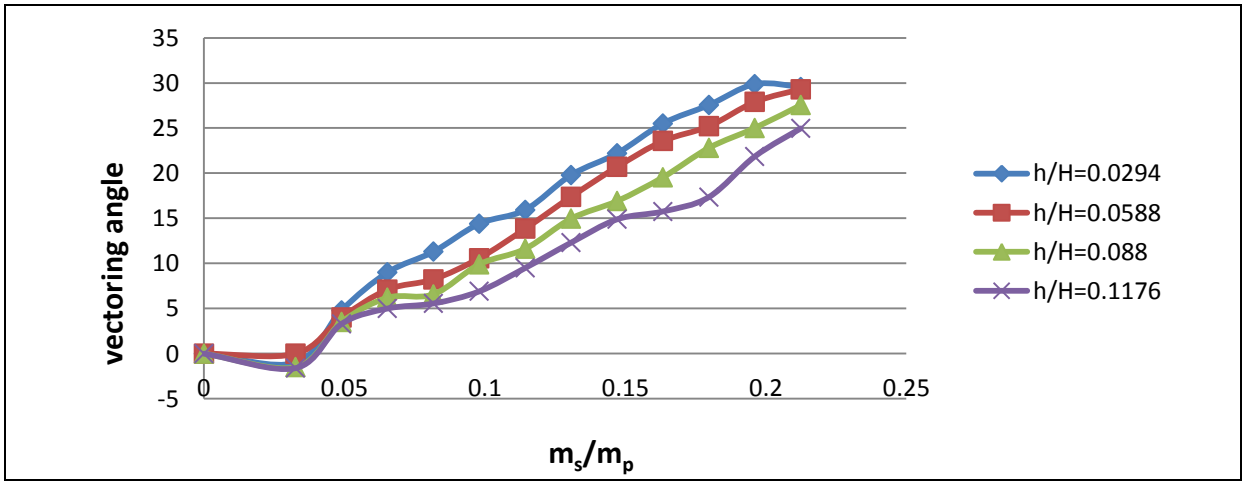

Figure 10: Experimental results of Thrust vectoring angle for varying secondary gap height at constant Coanda surface diameter Φ/H =2.353

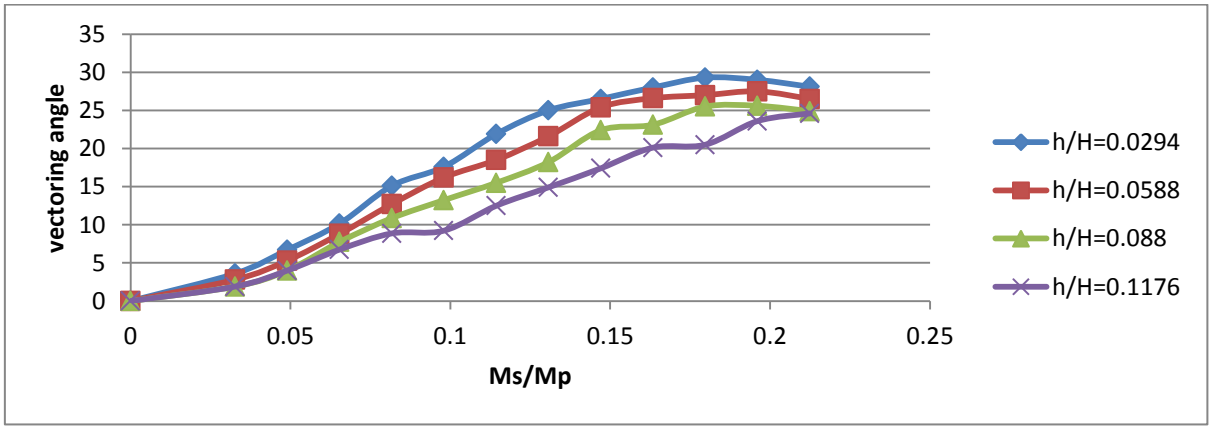

Figure 11: Experimental results of Thrust vectoring angle for varying secondary gap height at Constant Coanda surface diameter Φ/H =3.529

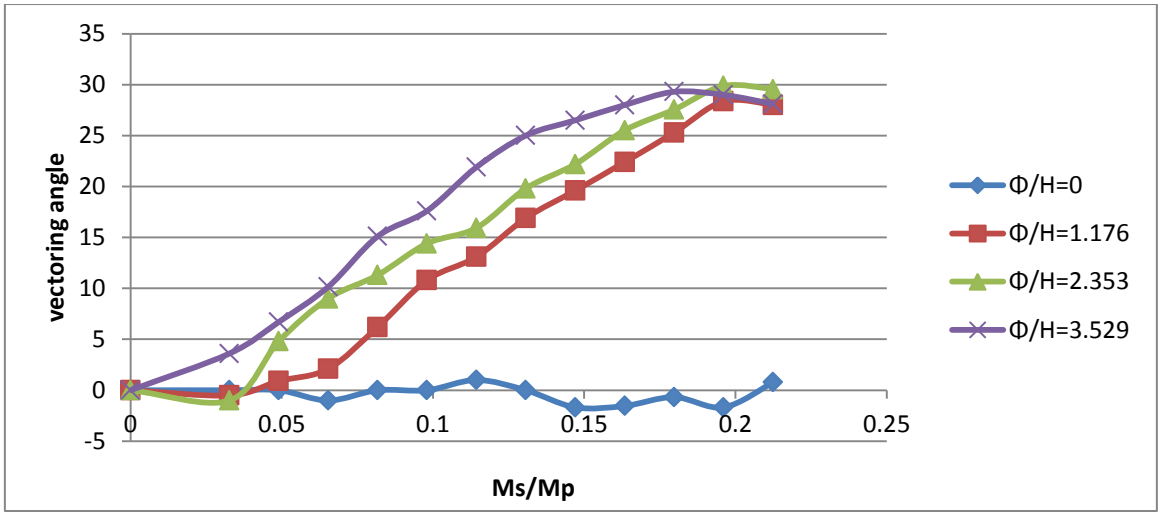

Figure 12: Experimental results of Thrust vectoring angle for varying Coanda surface diameter at Constant secondary gap height h/H=0.0294

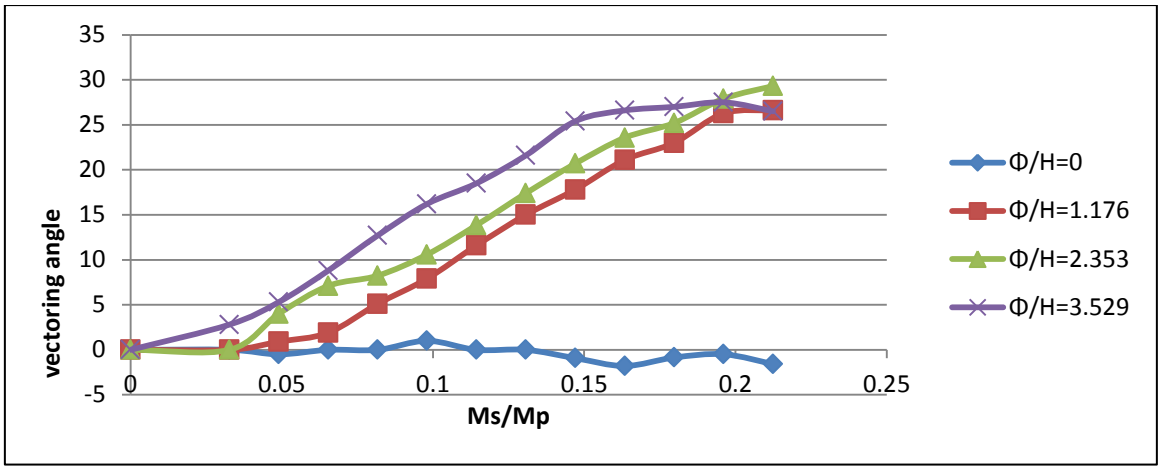

Figure 13: Experimental results of Thrust vectoring angle for varying Coanda surface diameter at constant secondary gap height h/H=0.0588

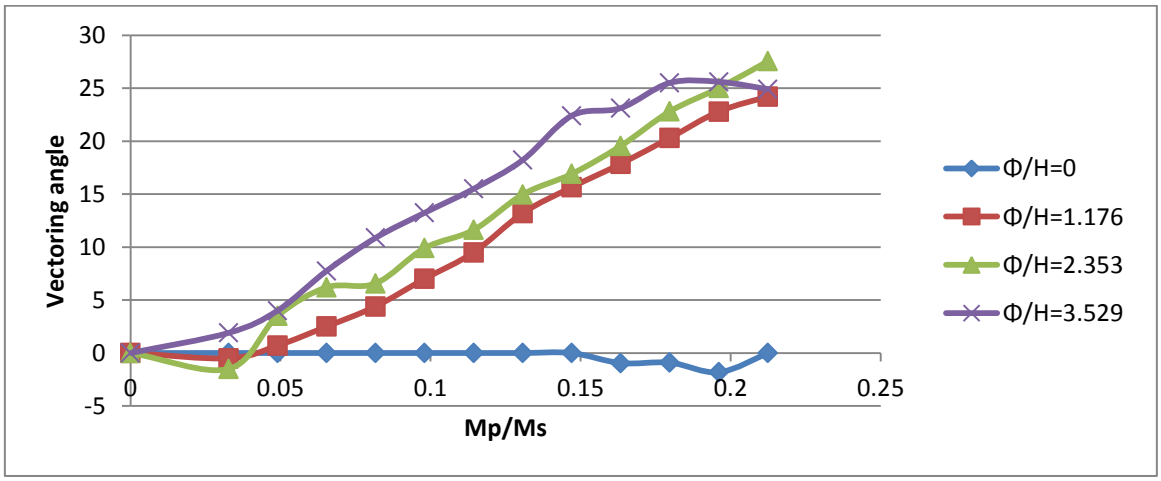

Figure 14: Experimental results of Thrust vectoring angle for varying Coanda surface diameter at constant secondary gap height h/H=0.088

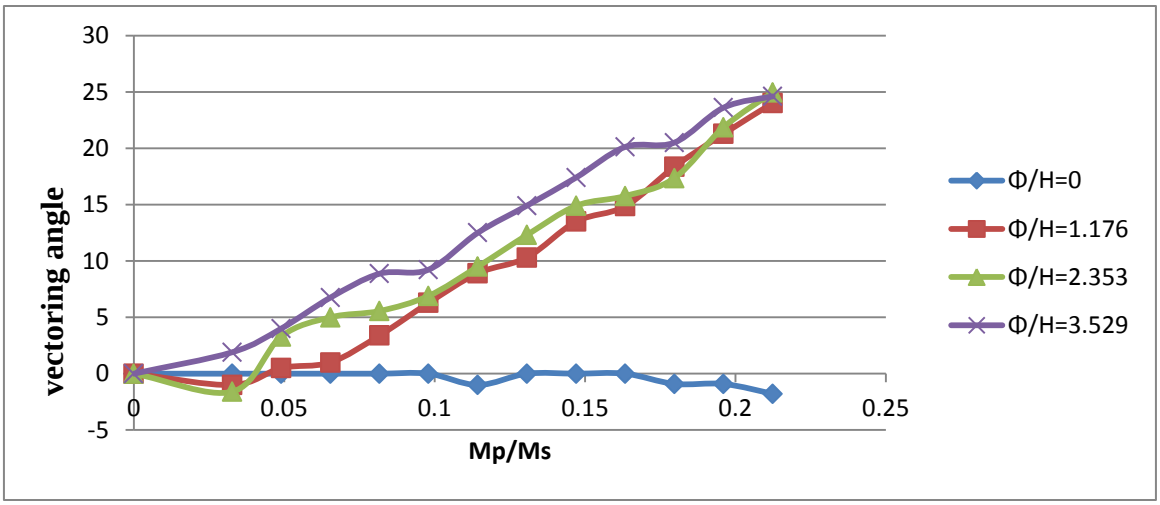

Figure 15: Experimental results of Thrust vectoring angle for varying Coanda surface diameter at Constant secondary gap height h/H=0.1176

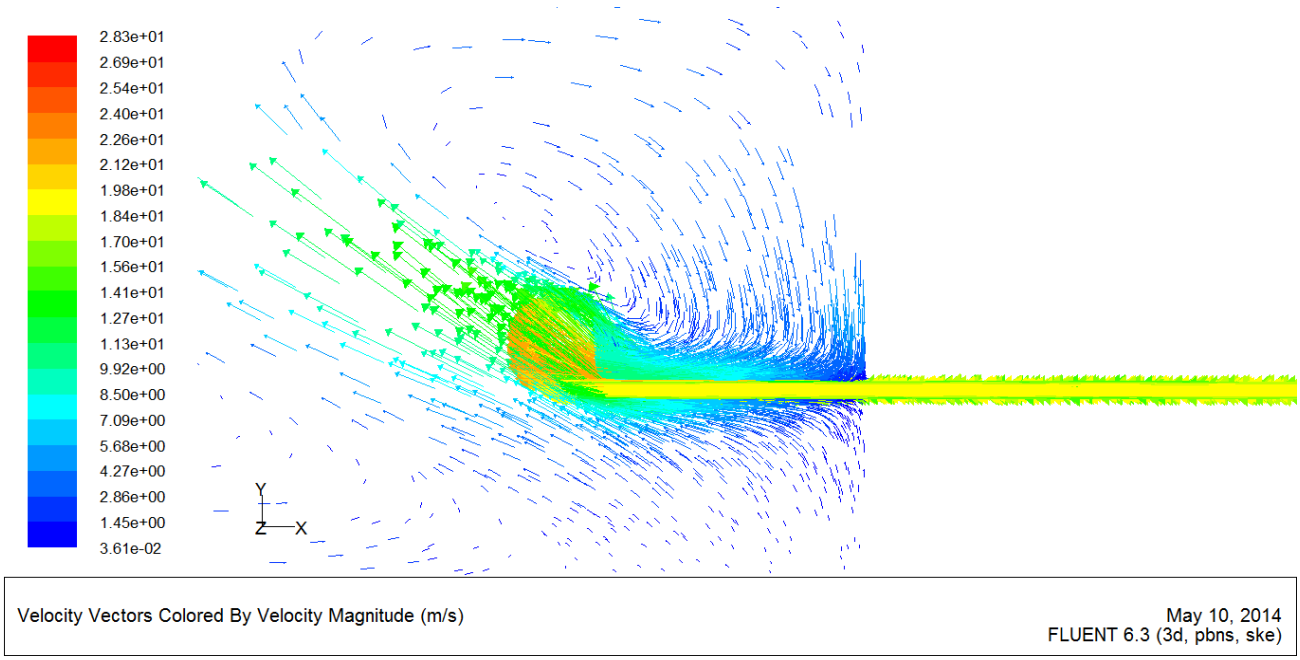

Figure 16: CFD simulation using FLUENT 6.3.26 showing Velocity vector at $\dot{m}s/\dot{m}p$ = 0.098, Φ /H=1.176 and h/H= 0.088

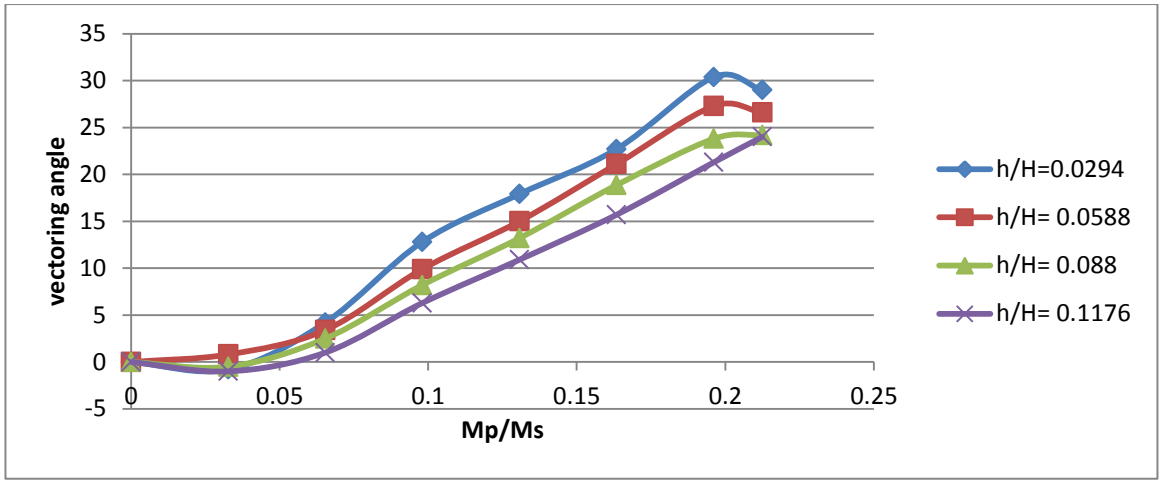

Figure 17: Theoretical results of Thrust vectoring angle for varying secondary gap height at constant Coanda surface diameter Φ/H =1.176

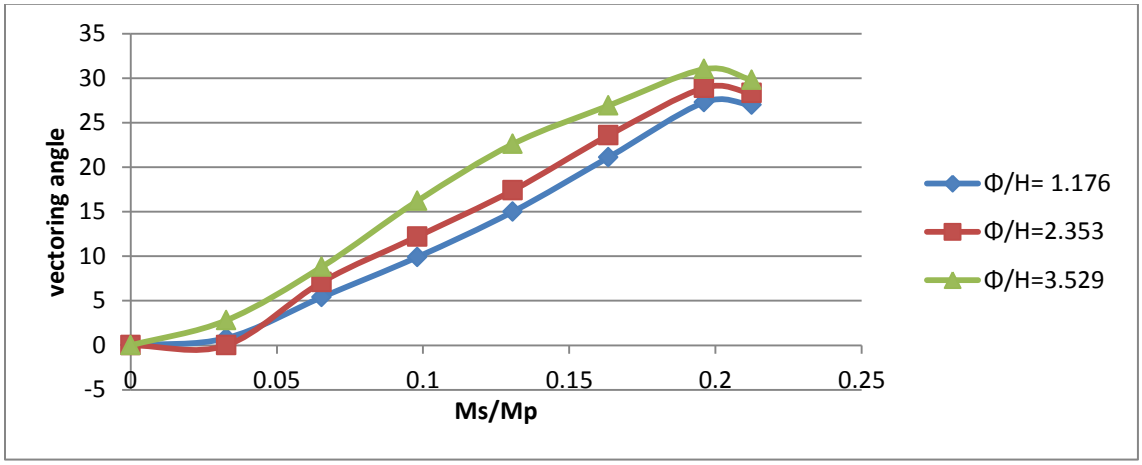

Figure 18: Theoretical results of thrust vectoring angle for varying Coanda surface diameter at constant secondary gap height h/H=0.0588

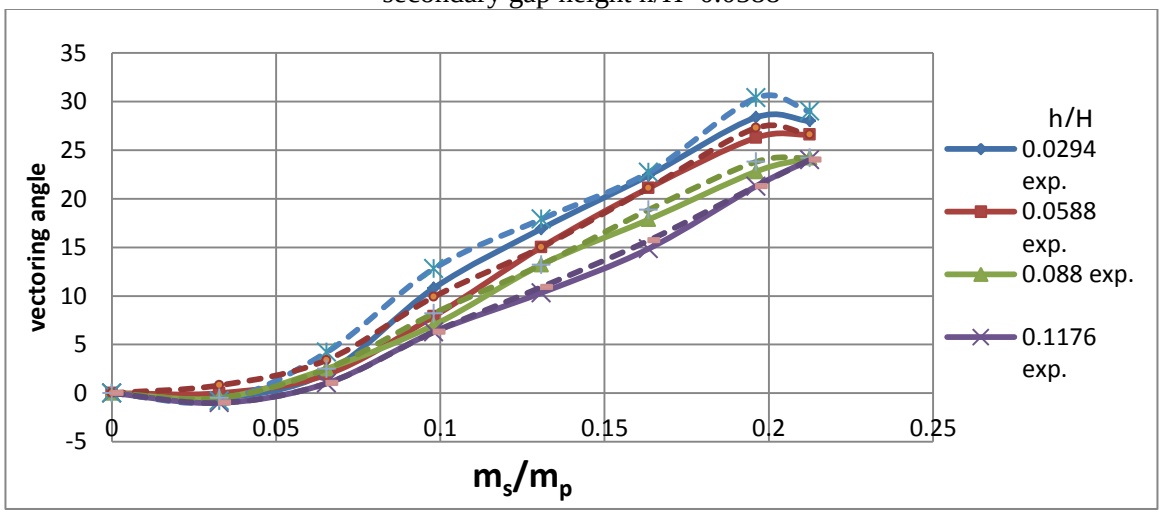

Figure 19: Comparison between CFD and Experimental result for varying secondary gap height at constant Coanda surface diameter Φ/H =1.176

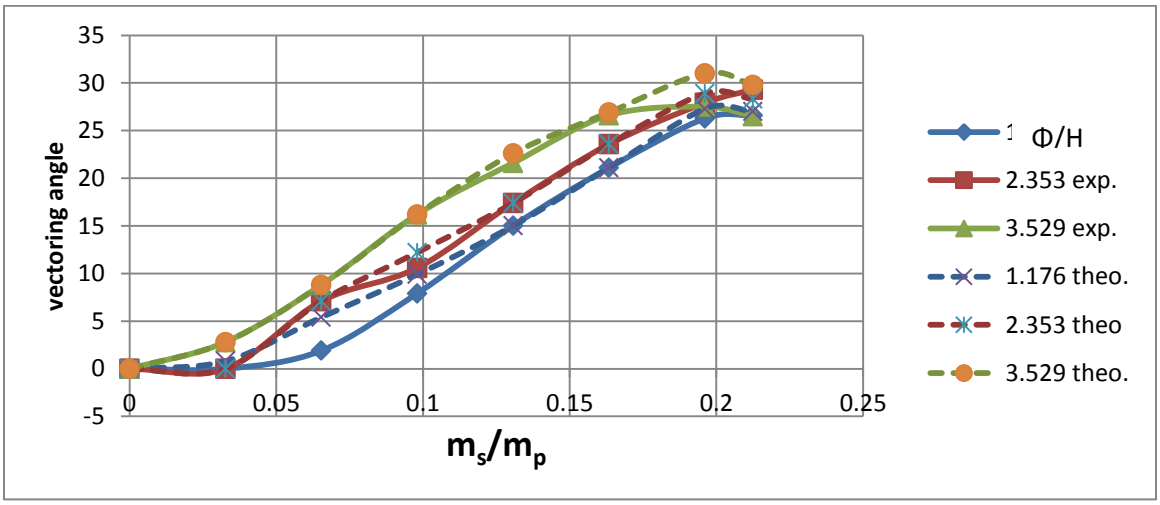

Figure 20: Comparison between theoretical and experimental result for varying Coanda surface diameter at constant secondary gap height h/H=0.0588

Table 1: The cases that have been tested in FLUENT

case	Φ/H	h/H	$\dot{m}s/\dot{m}p$						
			a	b	c	d	e	f	g
1	1.176	0.0294	0.03268	0.06536	0.098	0.1307	0.1634	0.196	0.2124
2	1.176	0.0588	0.03268	0.06536	0.098	0.1307	0.1634	0.196	0.2124
3	1.176	0.088	0.03268	0.06536	0.098	0.1307	0.1634	0.196	0.2124
4	1.176	0.1176	0.03268	0.06536	0.098	0.1307	0.1634	0.196	0.2124
5	2.353	0.0588	0.03268	0.06536	0.098	0.1307	0.1634	0.196	0.2124
6	3.529	0.0588	0.03268	0.06536	0.098	0.1307	0.1634	0.196	0.2124